# Size distribution of aggregates across different aquatic systems around Japan shows that stronger aggregates are formed under turbulence

**Marika Takeuchi** [1,2]* **Sarah L. C. Giering** [1] **Hidekatsu Yamazaki** [2,3,4]

[1]Ocean BioGeosciences, National Oceanography Centre, Southampton, Hampshire, UK
[2]Department of Ocean Sciences, Tokyo University of Marine Science and Technology, Minato-Ku, Tokyo, Japan
[3]School of Marine Sciences, Sun Yat-sen University, Shanghai, China
[4]Okinawa Institute of Science and Technology, Onna-son, Okinawa, Japan

## Abstract

Marine aggregates, composed of various particles, play a crucial role in ocean carbon storage. The overall size distribution of the aggregates (number size spectra) is controlled by the balance between aggregation and disaggregation processes. Turbulence has been proposed to facilitate both aggregation and disaggregation by increasing the collision rate of aggregates or sometimes directly tearing them apart. Predominant processes driven by turbulence typically depend on the level of turbulence—relatively weak turbulence is associated with aggregation while stronger turbulence promotes disaggregation. Aggregate strength also plays a key role, as strongly bonded aggregates can withstand turbulence better, leading to lower disaggregation rates. While the relationship between turbulence and aggregate strength has been studied numerically and experimentally, field measurements remain limited. Here, we compare our number size spectra to turbulence intensity from the field measurements across different environmental settings around Japan to determine the effect of turbulence on aggregate strength. We combined measurements from 10 sites with different environmental settings and observed the flatter slopes (higher net aggregation rate) and shifts in the intersection lengths with an increase of turbulence, while strong turbulence is typically linked with disaggregation. Our findings suggested that stronger aggregates are formed under stronger turbulence and the overall population of strong aggregates also increases with an increase of turbulence intensity. We also compared our number size spectra with three other confounding factors (fluorescence, salinity, and aggregate compositions) to confirm the effects of turbulence are dominant in our aggregate dynamics.

Sinking particles in the ocean are a major pathway for transporting carbon from the surface to the deep water, hence, they play a critical role in determining ocean carbon storage (Briggs et al. 2020; Ducklow 2001; Falkowski et al. 1998). Some large aggregates (commonly referred to as marine snow) are formed through flocculation of miscellaneous materials such as

phytoplankton, detritus, and fecal pellets, and typically have a higher sinking speed and higher carbon content than their source particles (Alldredge and Silver 1988; Alldredge et al. 1998). The contributions of large aggregates to the sinking carbon flux are therefore acknowledged to be disproportionately large compared to individually existing, smaller particles (Buesseler and Boyd 2009; Turner 2015). In addition to sinking carbon flux, large aggregates also contribute to the local food availability in some ecosystems, providing a food source for larger organisms (i.e., mesozooplankton, macrozooplankton, fish larvae, and small fish) while small aggregates may not be recognized as their food (Larson and Shanks 1996; Möller et al. 2012; Chow et al. 2019; Tsukamoto and Miller 2020). Since the size of an aggregate partly determines its sinking velocity and carbon contents (Alldredge 1998; Khelifa and Hill 2017) and who will eat it (e.g., fish larvae select their food according to the food size; Tsukamoto and Miller 2020), investigating aggregate size is crucial to accurately evaluate chemical and biological impacts of aggregates to the ecosystems.

Aggregate size in an environment is determined by the balance between the rate of aggregation (increase of size) and disaggregation (decrease of size) that involve multiple physical and biological mechanisms. Aggregation can occur through particle collisions and flocculation, which typically increases with higher particle concentration (Jackson 1990; Burd and Jackson 2009), increasing physical forces (e.g., Brownian motion, differential sedimentation and turbulence), and higher concentration of "glues" (e.g., Transparent Exopolymer Particles) that make particles "sticky" (Passow 2002). A special form of particle formation, which we do not include in the term "aggregation" here, is the repackaging of particles by zooplankton and fish, who often ingest smaller particles and release larger, typically denser fecal pellets (Turner 2015). Disaggregation occurs through biological and physical processes, for example, zooplankton and fish can directly break aggregates during feeding, leading to the release of smaller fragments ("fragmentation"; Lampitt et al. 1990; Giering et al. 2014) or dissolved matter ("sloppy feeding"; Hasegawa et al. 2001; Møller et al. 2003; Steinberg et al. 2004). High sediment load in aggregates can make aggregates fragile and increase disaggregation rate (Passow and De La Rocha 2006), and turbulence could stretch aggregates and tear them apart (Braithwaite et al. 2012; Takeuchi et al. 2019; Song et al. 2023).

For any ecosystem, the balance between aggregation and disaggregation across all particle sizes can be explored using number size spectra (sometimes referred to as size distributions), which relate the total particle abundance of a certain size to its size class (McCave 1984). Size is a useful parameter to constrain ecosystem dynamics because it can be easily measured using, for example, *in-situ* camera systems (Lombard et al. 2019), requires little taxonomic analysis, and can be implemented relatively easily in models (Blanchard et al. 2017). The slope of number size spectra generally decreases as larger aggregates are typically rarer (Kwong and Pakhomov 2021), and the relative steepness of the slope indicates whether large aggregates are relatively more abundant (flatter slopes; e.g., because of high aggregation rates) or less abundant (steeper slope; e.g., because of low aggregation rates or loss of particles through disaggregation) (Logan and Kilps 1995; Li et al. 2004; Dissanayake et al. 2018). In an open system, additional processes can also influence the slope by, for example, importing large particles through advection, influx or export of sinking particles, or non-steady-state conditions. We here treat our systems as steady-state systems and focus on turbulence.

Turbulence is involved in both aggregation and disaggregation, and is typically stronger in coastal inshore waters than in the pelagic offshore waters (Geyer et al. 2008; Smyth and Moum 2019). Stronger turbulence is typically associated with higher disaggregation rates (Winterwerp 2002), but may also affect the properties of aggregates that form, since stronger aggregates can better resist disaggregation. In this study, we combine observational measurements of aggregate sizes at a wide range of turbulence levels obtained within the depth range of 10–100 m across diverse environmental settings around Japan (coastal sites to offshore sites, as well as freshwater sites). This large and broad dataset additionally allows us to compare aggregate number size spectra across other factors (e.g., phytoplankton abundance and salinity), thus reducing their effect as confounding factors to better demonstrate the potential effect of turbulence on aggregation processes.

## Method

A microstructure profiler vertically collected physical and biological variables (shear - turbulence, turbidity, fluorescence, conductivity - salinity and temperature) at each of the 10 study sites to investigate potential drivers of aggregate dynamics. To explore aggregate dynamics, we simultaneously measured aggregate size and abundance from *in-situ* images, along with physical and biological variables.

### Study area

Field campaigns were conducted at 10 different locations around Japan over different seasons and aquatic systems (Table 1, Fig. 1): 2 campaigns at the Kuroshio (2009 and 2013), 2 campaign at islands located at south of Japan (Oshima and Miyake) where the Kuroshio has strong influences on the water properties, 4 campaigns along the coast facing to the Pacific Ocean (Tokyo Bay in September and February, Tateyama, Jogashima and Otsuchi), and 1 campaign at the largest freshwater lake of Japan (Lake Biwa). Observations were carried out from R/T/V Seiyomaru (Tokyo University of Marine Science and Technology), R/V Kaiyo (JAMSTEC) and R/V Hakken (Lake Biwa Environmental Institute). Water column depths ranged from $\sim 30$ m (Tateyama and Otsuchi) to $\sim 5700$ m in the Kuroshio, and we sampled to a maximum depth of 10–100 m at each site.

Kuroshio transports warm and saline water from south to north of the Pacific Ocean and its oligotrophic water is typically dominated by the pico- and nano-phytoplankton community (Clayton et al. 2014). It is also widely acknowledged as a spawning and nursery grounds of a variety of fish despite insufficient nutrient supplies (Nagai et al. 2019). Along the coast, phytoplankton communities are typically dominated by larger phytoplankton (often diatoms and dinoflagellates) with overall higher primary production (Han and Furuya 2000; Ramaiah and Furuya 2002; Tachibana et al. 2016). Furthermore, a significant influence of tidal flow on transporting suspended particles and sediment resuspension has been observed at the baymouth of Tokyo Bay (Arakawa et al. 2003) and Otsuchi Bay (Masunaga et al. 2017). Lake Biwa is one of the major water supplies in the western region of Japan, and eutrophication and change of ecological dynamics due to the environmental changes has been suggested by the historical monitoring (Tsugeki et al. 2009). In our study, we refer to Lake Biwa data to compare freshwater systems with oceanic systems.

**Table 1.** Details of observation sites. Sites are grouped according to the location and the position relative to Kuroshio. Number of profiles at each location varied between 1 and 23 collected on one night at each site (except for Kuroshio 2009 and Kuroshio 2013, where profiles were collected over 1 week). Temperature (Temp), salinity (Sal), turbidity (Turb), fluorescence (Fluo) and TKE dissipation rate ($\varepsilon$) are averages and standard deviations throughout the study period over the sampling depth range.

| Group | Site | Year | M | Lat. (°N) | Lon. (°E) | Echo depth (m) | Sampling depth range (m) | Temp (°C)* | Turb (ppm)* | Sal (PSU)* | Fluo (mg m⁻³)* | Log10($\varepsilon$) (W kg⁻¹)* |
|---|---|---|---|---|---|---|---|---|---|---|---|---|
| Kuroshio | Kuroshio | 2009 | Oct | 35.07 | 142.91 | 5700 | 0–100 | 22.9 ± 2.1 | 0.35 ± 0.05 | 34.3 ± 0.2 | 0.17 ± 0.17 | −8.38 ± 0.94 |
| | Kuroshio | 2013 | Jul | 36.14 | 146.31 | 5700 | 0–100 | 21.4 ± 2.5 | 0.29 ± 0.06 | 34.5 ± 0.2 | 0.94 ± 1.36 | −8.94 ± 0.87 |
| Kuroshio Islands | Miyake | 2012 | May | 34.04 | 139.47 | 266 | 0–100 | 18.7 ± 1.2 | 0.49 ± 0.11 | 35.0 ± 0.1 | 0.88 ± 0.80 | −7.25 ± 0.82 |
| | Oshima | 2013 | Jun | 34.70 | 139.50 | 899 | 0–60 | 19.9 ± 1.1 | 0.45 ± 0.13 | 34.4 ± 0.1 | 2.94 ± 5.07 | −8.11 ± 086 |
| Coast | Otsuchi | 2013 | Sep | 39.34 | 141.93 | 28 | 0–20 | 22.1 ± 0.5 | 0.94 ± 0.17 | 33.6 ± 0.1 | 3.63 ± 1.31 | −8.49 ± 0.40 |
| | Jogashima | 2011 | Jun | 35.12 | 139.64 | 49 | 0–40 | 18.4 ± 1.1 | 1.24 ± 0.63 | 33.0 ± 1.2 | 2.19 ± 2.69 | −7.37 ± 0.82 |
| | Tateyama | 2014 | May | 35.01 | 139.83 | 29 | 0–20 | 19.0 ± 0.7 | 1.50 ± 0.63 | 34.5 ± 0.1 | 7.56 ± 7.77 | −7.39 ± 0.95 |
| | Tokyo Feb | 2008 | Feb | 35.27 | 139.72 | 67 | 0–60 | 10.5 ± 0.4 | 2.08 ± 0.35 | 33.2 ± 0.2 | 1.13 ± 1.47 | −6.78 ± 1.02 |
| | Tokyo Sep | 2012 | Sep | 35.28 | 139.72 | 67 | 0–60 | 21.8 ± 3.1 | 1.71 ± 0.25 | 33.6 ± 1.0 | 1.60 ± 1.55 | −7.58 ± 0.72 |
| Lake | Biwa | 2010 | Aug | 35.39 | 136.10 | 91 | 0–80 | 12.0 ± 6.8 | 0.78 ± 0.40 | 0.00 | 0.27 ± 0.25 | −8.95 ± 0.77 |

Since our study sites were located in such unique environments, we grouped 10 campaigns into four groups based on the location to evaluate the difference across the environments. The offshore locations in Kuroshio (2009 data and 2013 data) were grouped as "Kuroshio." Miyake and Oshima, the islands located at the Pacific Ocean (179 and 120 km off of the Japanese coast, respectively) and have the water properties influenced by the Kuroshio, were grouped as "Kuroshio Islands." Otsuchi, Tateyama, Jogashima, and Tokyo Bay (in Feb and Sep) were grouped as "Coast" owing to their close proximity to the coast, and finally Lake Biwa was categorized as "Lake."

**Physical and biological measurements**

A free fall microstructure profiler (TurboMAP-L, JFE Advantech Co., Ltd.) was deployed to measure turbulent velocity shear, temperature, conductivity, turbidity, and fluorescence at a sampling rate of 512 Hz with a fall-speed of $\sim$ 0.5 m s⁻¹ (Doubell et al. 2009).

*Turbulence*

Turbulent kinetic energy (TKE) dissipation rate ($\varepsilon$, W kg⁻¹), indicating how much kinetic energy is dissipated to heat (hence indicating the intensity of turbulence), was estimated by integrating the turbulent velocity shear spectrum over 2 s segment from approximately 1 cycle per meter to half the Kolmogorov wavenumber. The Kolmogorov wavenumber, $k$, is

$$k = \left(\frac{\nu^3}{\varepsilon}\right)^{1/4},$$ (1)

where $\nu$ is the kinematic viscosity of seawater. The Nasmyth empirical spectrum (Nasmyth 1970) was applied to recover unresolved variance (Doubell et al. 2009; Kokubu et al. 2013). The Kolmogorov length scale, $L_k$, which is the smallest eddy scale:

$$L_k = \left(\frac{\nu^3}{\varepsilon}\right)^{1/4}.$$ (2)

*Fluorescence*

TurboMAP-L carried two fluorescence probes with (1) LEDs light source (Nichia NLPB310, 400–480 nm waveband) with a vertical resolution of $\sim$ 2 cm (Wolk et al. 2001, 2002, 2006) and (2) a laser light source (Nichia NDHB510APA, peak wavelength = 410 nm) with a vertical resolution of $\sim$ 2 mm (Doubell et al. 2009). The laser fluorescence probe with high spatial resolution acquired significantly strong spike signals that we did not observe in LED fluorescence data (Supporting Information Fig. S1a). We averaged both LED fluorescence and laser fluorescence over 1-m depth bins to confirm the spike signals of laser fluorescence were natural signals and likely detecting fluorescent aggregates as observed in backscatter and
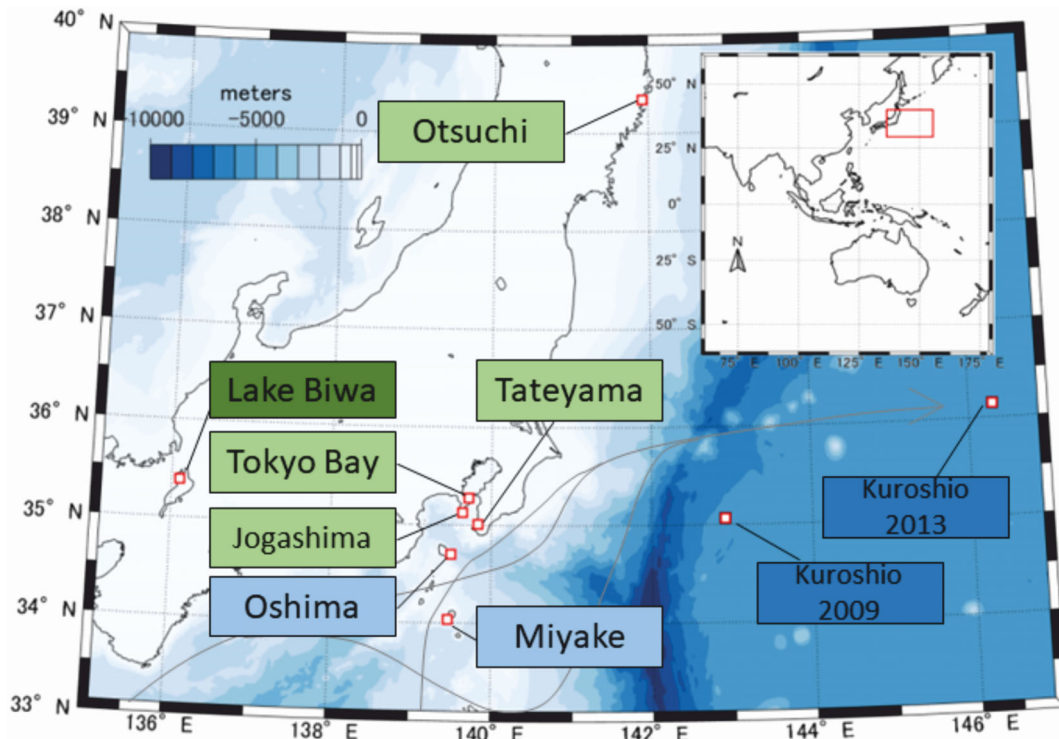
**Fig. 1.** Observation sites. The colors of the text boxes indicate the site grouping: dark blue is "Kuroshio," light blue is "Kuroshio islands," light green is "coast," and dark green is "lake." Gray arrow indicates the path of the Kuroshio. Sites are overlaid on the bathymetry of the region as indicated by the color scale.

fluorescent measurements (Briggs et al. 2011). We therefore separated the spike signals of laser fluorescence (proxy for mm scale fluorescent aggregates) from the background signal (1.5 times of 1-m moving average) of laser fluorescence (proxy for small fluorescent particles) (Foloni-Neto et al. 2014, 2016). To directly compare fluorescence with total aggregate volume concentration (fraction of aggregate volume to sampled water volume), which is calculated over a 10-m depth bin (*see* also Eq. (4)), we also binned fluorescence over 10-m depth bins. In order not to lose the features of high spatial resolutions that can separate fluorescent aggregates and small particles, we integrated fluorescence signals by trapezoidal method instead of taking average. Hence, integrated spike signals for every 10 m depth, hereafter referred to *Fluorescence-Spikes* in mg m$^{-2}$, is a proxy of fluorescent aggregate abundance over 10 m. Integrated entire fluorescence signals (spikes and background) for every 10 m is a proxy of total fluorescent abundance within the depth bin, hereafter referred to *Fluorescence-Total* in mg m$^{-2}$.

### Turbidity and proxy for sediment load

Intensity of light backscatter from suspended particles as a measure of turbidity was measured using the same source as the LED fluorescence probe (Nichia NLPB310, 400–480 nm waveband). As we did not have direct measurements of sediment load at our sampling sites, we used the ratio of

fluorescence to turbidity (sediment load: nonfluorescent turbidity $\sim 1 -$ fluorescence/turbidity) as a proxy. Note that this proxy is relatively crude as it assumes that particles that are not fluorescent are inorganic.

### Salinity and temperature

Conductivity (ms) and temperature ($^{\circ}$C) are measured with a platinum wire thermometer and an inductive conductivity cell, and salinity was calculated from conductivity and temperature. Average temperature and salinity were calculated using all measurements at each site.

### Aggregate images and derived properties

We mounted a mini CMOS camera (DSL II 190, Little Leonard Inc.) on the TurboMAP-L to collect images of aggregates—57,669 images were collected over 148 profiles in total. The camera was fitted at 10 cm away from the LED fluorescence probe to use the illumination from LED fluorescence probe (460 nm, blue). Images were sampled at 5 Hz in the direction of travel—facing downwards, which is equivalent to an image every 10 cm. All images were recorded in RGB color (1024 × 1280 pixels, pixel resolution of 59 $\mu$m). We cropped the brightest regions of the images (the region close to the light is bright) into a field of view with 2 cm × 2 cm, providing sampling volume $\sim 8$ cm$^3$/image for further analysis. The blue channel of each image was selected and the brightness

balance across the image was corrected by subtracting the background image (average of multiple images).

Streaked images were identified by assessing the 2D image spectrum using a 2D Fast Fourier Transform (2D FFT) (Franks and Jaffe [2001]; Doubell et al. [2009]). When images are not smeared, the 2D spectrum is a symmetric circle, whereas for streaked images, asymmetry is seen in the 2D spectrum. To test for asymmetry, two perpendicular sets of 1D spectra from 2D spectrum (i.e., a *x*-axis and *y*-axis contour plot) were chosen, and the ratio of variance for each wavenumber was calculated for each perpendicular pair. The variance ratio is approximately 1 in unstreaked images, with images rejected from further analysis if the average variance ratio for one perpendicular pair exceeded 1.5 or 1/1.5 (Franks and Jaffe [2001], [2008]; Doubell et al. [2009]). This criterion assesses smearing across all aggregates imaged in the field of view and minimizes the rejection of images that contain rare individual long and thin aggregates. We carried out a sensitivity analysis using lower and upper ratios of 1.4 or 1/1.4 and 1.6 or 1/1.6 and found that aggregate size distributions (i.e., slopes of aggregate number size spectra—described in the next section) were not significantly (ANCOVA) affected by the streak metric. Additional laboratory tank experiments using particles of known size were conducted to confirm that unfocused particles and streaked images were removed by the size threshold and 2D spectrum criteria.

Screened images were binarized using Otsu thresholding methods and individual aggregates were then approximated as ellipses using the *regionprops* function in MATLAB (R2022a Mathworks Inc.) to determine the aggregate sizes (major axis length, *MajAL*, in cm; equivalent spherical diameters, *ESD*, in cm). To test whether the choice of thresholding algorithm affects our aggregate size distributions, we also applied Sobel and Canny thresholding algorithms to binarize images and found no significant difference in the slopes (ANCOVA). To focus on the larger size fraction of aggregates expected to be influenced by turbulence (McCave [1984]), only objects with *MajAL* > 0.03 cm were considered as our target aggregates. Volume of an individual aggregate as $V_{ind}$ was estimated from the following equation:

$$V_{ind} = \frac{\pi}{6} ESD^3. \tag{3}$$

The total volume concentration of aggregates for every 10 m (i.e., 0–10 m, 10–20 m, 20–30 m depth, etc.), the fraction of water volume occupied by aggregates, $V_{agg}$, was calculated:

$$V_{agg} = \frac{\text{Sum of } V_{ind}}{\text{Sample volume for 10 m}}. \tag{4}$$

Since DSL camera captures ~ 10 images m$^{-1}$, we selected 10-m depth bins to obtain a sufficient number of images of

aggregates to calculate $V_{agg}$. The unit of $V_{agg}$ is in cm$^3$ m$^{-3}$, which is equivalent to parts per million, ppm.

## Number size spectra

In this study, we are using number size spectra (Petrik et al. [2013]) to describe our aggregate size distribution, and the results are comparable to past model outputs and field measurement. The number of aggregates, $N_{agg}$, in logarithmically increasing *MajAL*-bins was calculated using all aggregates in each group (Kuroshio, Kuroshio island, Coast and Lake). $N_{agg}$ was divided by the bin width ($\Delta MajAL$) and the sample volume ($V_{im}$) to obtain normalized aggregate abundance ($n = \frac{N_{agg}}{\Delta MajAL}/V_{im}$), and $\log_{10}(n)$ was plotted against the logarithm of the average bin size ($\log_{10}(\overline{MajAL})$) to construct a number size spectrum. Any bin with the insufficient number of aggregates $N < 10$ was discarded before computing the spectrum. We noticed a change in the slope within each number size spectrum, and hence fitted a bilinear regression using the least squares method. To do so, we fitted a series of two slopes to each number size spectrum with the breaks varying from the second to the second-last bin; that is, a slope from 1$^{st}$ bin to *i*-th bin (slope of small aggregates) and another slope from *i*-th bin to the last bin (slope of large aggregates). We calculated the sum of mean squared errors of each pair of slopes, and the best-fit slopes were established when the error was smallest.

Following this operation, we constructed number size spectra for individual sites, location groups and turbulence levels. For the individual sites, we used all the images that were collected at the site, so that the number size spectra show the aggregate size distribution through the water column at the site. For the location groups, we merged the images from the sites that are in the same group to construct number size spectra. For example, to construct the number size spectrum of Kuroshio in 2009 and Kuroshio in 2013, hence the number size spectrum describes the general trend of aggregate size distribution from the location group. Finally, we constructed number size spectra for six different levels of turbulence kinetic energy dissipation rate ($10^{-11} < 10^{-10}$, $10^{-10} < 10^{-9}$, $10^{-9} < 10^{-8}$, $10^{-8} < 10^{-7}$, $10^{-7} < 10^{-6}$, $10^{-6} < 10^{-5}$ W kg$^{-1}$) using the raw data across all 10 sites to investigate the universal influences of turbulence on aggregate dynamics regardless of locations (variation of turbulence kinetic energy dissipation rate measured at each site is shown in Supporting Information Fig. S2). The reason for the turbulence bins is that the calculation of a full number size spectrum requires a large number of aggregates. In our case, we needed more than > 10,000 aggregates per spectrum. We carried out ANCOVA and found that the slopes of number size spectra across six levels of turbulence kinetic energy dissipation rates are significantly different.

## Statistical analyses

The relationship between the number size spectra slopes of the aggregates (both small and large) and different

environmental parameters was explored using simple linear regression in R (v4.3.2).

## Results

### Biological and physical variability for location group

Water mass properties showed Kuroshio and Kuroshio Islands had relatively higher salinity water (34.1–35.1 PSU; Supporting Information Table S1; Fig. S3), compared to Coast (31.2–34.7 PSU). Similar water mass properties between Kuroshio and the Kuroshio Islands indicated a strong influence of the Kuroshio on the island region. However, biological and physical variables (fluorescence, turbidity, aggregate volume concentration, and turbulence) were relatively lower at the Kuroshio Islands (Fig. 2; Supporting Information Table S2). Temperature did not show clear trend between different groups because of the seasonal variations (Supporting Information Table S1). Overall, at the oceanic location groups, biological and physical variables generally decreased from inshore (Coast) toward offshore (Kuroshio). Lake Biwa exhibited lower biological and physical variables than the oceanic locations, highlighting the difference between freshwater and oceanic systems.

*Fluorescence-Total* (a proxy of total fluorescence biomass for 10 m depth bins) and *Fluorescence-Spikes* (a proxy of fluorescent aggregate biomass in 10 m depth bins) showed similar trends. *Fluorescence-Total* ranged from $10^{1.8}$ mg m$^{-2}$ to $10^{3.4}$ mg m$^{-2}$, while *Fluorescence-Spikes* ranged from $10^{-0.3}$ mg m$^{-2}$ to $10^{4.1}$ mg m$^{-2}$ (Fig. 2a,b; Supporting Information Table S2). At the oceanic sites, maxima for both proxies were highest at the Coast and decreased offshore. Average fluorescence (both proxies) was similar at the Coast and Kuroshio Islands, and lower in the Kuroshio. This trend matches previously reported seasonal averages ($\sim 10^{-1}$ mg m$^{-2}$ for the Kuroshio and $\sim 10^{2}$ mg m$^{-2}$ for coastal waters, Wang et al. 2011). The lowest maxima and medians for both proxies were observed at Lake Biwa site (Fig. 2a,b; Supporting Information Table S2).

The ratio between *Fluorescence-Spike* to *Fluorescence-Total* (indicating the contribution of fluorescent aggregate biomass to total fluorescent particle biomass) ranged from 0.1% to 45.3% across all sites, with a decreasing trend from coast to offshore and overall lowest values for Lake Biwa (Fig. 2c; Supporting Information Table S2). The highest contribution of *Fluorescent-Spikes* (both maximum and median) was found at the Coast. Site-specific maxima were 26.9% for Kuroshio Islands and 29.0% for Kuroshio, showing no clear decrease with the distance from the coastline, while site-specific medians showed the typical decrease offshore. The lowest site-specific maximum was, again, at Lake Biwa (17.4%).

Both turbidity and $V_{agg}$ showed similar trends. Turbidity ranged between $10^{-1}$ and $10^{1}$ ppm across all sites, with median values of $10^{-0.5}$ ppm (Kuroshio), $10^{-0.4}$ ppm (Kuroshio Islands), $10^{0.2}$ ppm (Coast) and $10^{-0.1}$ ppm (Lake Biwa) (Fig. 2d; Supporting Information Table S2). Total

volume concentration of aggregates ($V_{agg}$) ranged between $10^{1}$ and $10^{3.6}$ ppm across all groups (Fig. 2e; Supporting Information Table S2). In the oceanic systems, turbidity and $V_{agg}$ (both median and maximum) was highest at the Coast. Median levels decreased offshore, but group-specific maxima did not. Lake Biwa had the second highest median turbidity and $V_{agg}$, and the overall highest turbidity. Turbulence kinetic energy (TKE) dissipation rate ranged from $10^{-10.6}$ to $10^{-4.7}$ W kg$^{-1}$ with wide variation across all sites (Fig. 2f,g). Turbulence was highest (both median and maximum) at the Coast, with similar levels at the Kuroshio Islands. The offshore Kuroshio had on average lower turbulence yet the highest range. Lake Biwa experienced the lowest median turbulence (Supporting Information Table S2).

### Comparison between aggregate volume and fluorescence

We related *Fluorescence-Spikes* (a proxy of fluorescent aggregate biomass, mg m$^{-2}$) with the total volume concentration of aggregates ($V_{agg}$, ppm) to investigate the fluorescent contents of aggregates across different locations (Fig. 3a). *Fluorescence-Spikes* and $V_{agg}$ were not significantly correlated in the Kuroshio ($p = 0.09$, $R^2 = 0.01$, $n = 185$), potentially owing to two distinct particle populations. For the other locations, there was a significant positive correlation, albeit with a high degree of scatter (Kuroshio Islands: $p < 0.01$, $R^2 = 0.01$, $n = 164$; coast: $p < 0.01$, $R^2 = 0.2$, $n = 239$; lake: $p < 0.01$, $R^2 = 0.29$, $n = 62$). Across all locations, *Fluorescence-Spikes* and $V_{agg}$ were significantly positively correlated, though $V_{agg}$ was a relatively poor predictor ($R^2 = 0.19$, $p < 0.01$, $n = 650$). Notably, the Kuroshio islands had similar *Fluorescence-Spikes* levels to the Coast despite much lower $V_{agg}$, indicating that particles here had a higher fluorescence content.

### Number size spectra

Across the location groups, normalized aggregate abundance ($n$) as a function of size (*MajAL*, cm) ranged from $8.5 \times 10^{-4}$ to $8.2 \times 10$ cm$^{-4}$, and decreased with increasing size (*MajAL*, cm) (Fig. 3b). In the Kuroshio, normalized aggregate abundance was the lowest of the four groups ($8.5 \times 10^{-4}$ to $2.8 \times 10$ cm$^{-4}$ for *MajAL* > 0.05 cm). In addition, the bilinear slopes of the number size spectra were the steepest of all four groups (Table 2). At the Kuroshio Islands, normalized aggregate abundance were higher than in the Kuroshio ($3.3 \times 10^{-3}$ to $1.7 \times 10$ cm$^{-4}$), and the number size spectra slopes were less steep (Table 2). At the Coast, normalized aggregate abundance was highest ($7.6 \times 10^{-2}$ to $8.2 \times 10$ cm$^{-4}$) with the flattest number size spectra slopes (Table 2). In Lake Biwa, the normalized aggregate abundance had the highest range ($6.3 \times 10^{-3}$ to $7.4 \times 10$ cm$^{-4}$) and steep number size spectra slopes (Table 2).

The flattest slopes were found at Tokyo Bay in February for both small and large aggregates (respectively, −1.37 and −3.53; Supporting Information Table S3; Fig. S4). The steepest slope of small aggregates was in the Kuroshio in 2013 (−2.97),
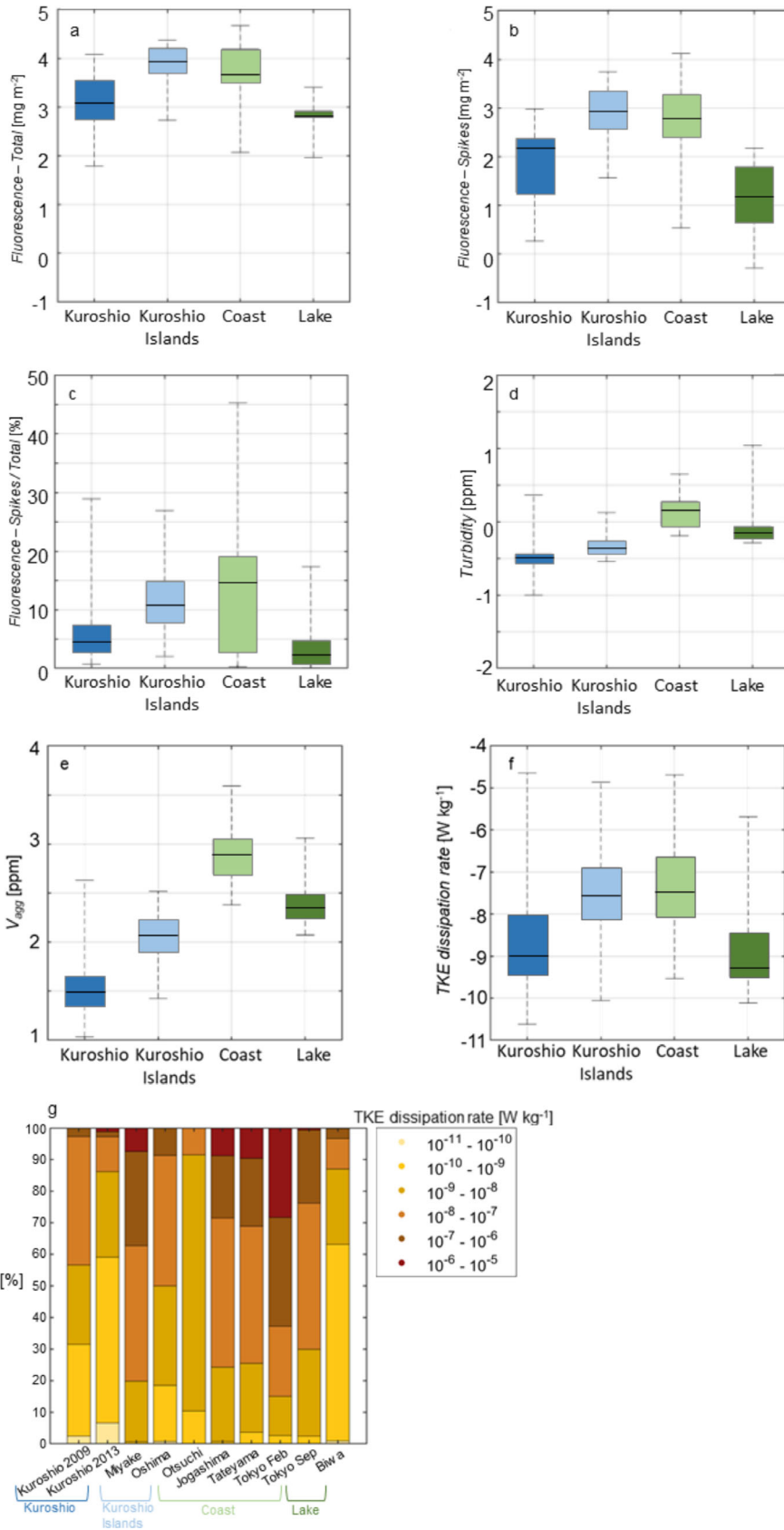
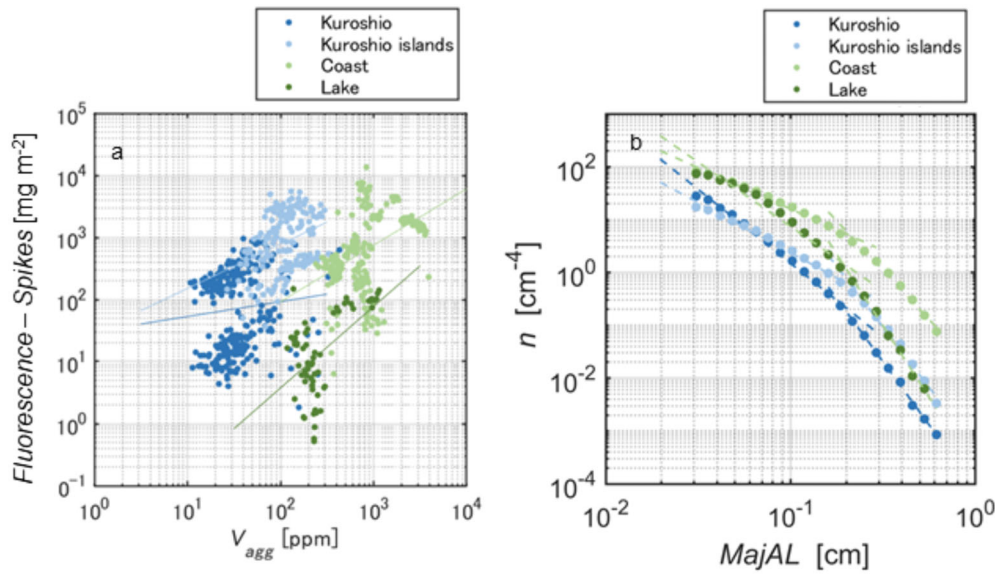*(Figure legend continues on next page.)*

**Fig. 3.** (a) Relationship between integrated (10-m bins) fluorescence of aggregates (*Fluorescence-Spikes*, mg m$^{-2}$) and total volume concentration of aggregates (*V*$_{agg}$, ppm). Lines show regressions (*see* the text for statistics). (**b**) Number size spectra-normalized aggregate abundance (*n*, cm$^{-4}$) as a function of size (*MajAL*, cm) for each group. The dots represent aggregate abundance (number of aggregates in each bin size divided by the bin width, *n*, cm$^{-4}$), and the dashed lines indicate bilinear regression lines of each spectrum. Colors indicate location groups corresponding to Fig. 1 (dark blue is Kuroshio, light blue is Kuroshio Islands, light green is coast, and dark green is lake).

while the steepest slope for large aggregates was at Miyake (−5.71). The slopes of the number-size spectra in Tokyo Bay were shallower during winter (−1.37 for small aggregates and −3.53 for large aggregates) compared to summer (−1.81 for small aggregates and −4.08 for large aggregates).

Overall, our number size spectra slopes had a slightly wider range (−1.37 to −5.71; Table 2; Supporting Information Table S3) than previous field measurements (−2 to −5, Table 1 in Omand et al. 2020). However, our range nicely brackets the

previous measurements, and hence appears realistic. The slight discrepancy may be due to methodological differences: Omand et al. (2020) used equivalent spherical diameter to calculate bin sizes, while we used major axis length.

### Number size spectrum characteristics in relation to turbulence

Our number size spectra for different levels of turbulence kinetic energy dissipation rate (*ε*, TKE dissipation rate, W

**Table 2.** Bilinear regression lines of number size spectra and aspect ratio spectra for each location group. Size spectra intersection length describes the aggregate size where the slopes of small and large aggregates meet. The total number of particles to compile the spectra is included.

| | Group | Slope of small aggregates | Slope of large aggregates | Intersection length (*MajAL*, cm) | Number of aggregates |
|---|---|---|---|---|---|
| Number size spectra | Kuroshio | −2.80 | −4.79 | 0.19 | 276,200 |
| | Kuroshio islands | −1.89 | −4.58 | 0.21 | 120,440 |
| | Coast | −1.56 | −3.73 | 0.21 | 735,749 |
| | Lake | −2.44 | −5.42 | 0.19 | 161,608 |

*(Figure legend continued from previous page.)*

**Fig. 2.** Comparison of biological and physical variables across location groups (Kuroshio, Kuroshio Islands, Coast, and Lake). Boxplots show maximum, 75th percentile, median, 25th percentile and minimum for (**a**) *Fluorescence-Total* (mg m$^{-2}$), (**b**) *Fluorescence-Spikes* (mg m$^{-2}$), (**c**) ratio between aggregate fluorescence relative to total fluorescence (*Fluorescence-Spikes /Fluorescence-Total*) (%), (**d**) 1-m averaged turbidity (ppm), (**e**) total volume concentration of aggregates *V*$_{agg}$ (10-m bins) (ppm), (**f**) turbulent kinetic energy (*TKE*) dissipation rate (1-m average) (W kg$^{-1}$), (**g**) ratio of different levels of TKE dissipation rate. Colors in (**a–f**) indicate the location group (corresponding to Fig. 1). Dark blue is Kuroshio, light blue is Kuroshio islands, light green is coast, and dark green is lake. Colors in (**g**) indicate turbulence levels as shown in legend.

kg$^{-1}$) (Fig. 4b; Supporting Information Table S4), constructed using all non-averaged data from the 10 locations, show the influences of turbulence on aggregate dynamics regardless of locations. For the weakest turbulence bin ($10^{-11} < \varepsilon$ $<10^{-10}$ W kg$^{-1}$), a full spectrum was not obtained due to an insufficient number of aggregates in the largest size bins (*MajAL* > 0.36 cm). Normalized aggregate abundance (*n*,

cm$^{-4}$) increased with higher turbulence levels (Fig. 4b; Supporting Information Table S4). In line with this observation, the median of total volume concentration of aggregates ($V_{agg}$, ppm) also increased with increasing turbulence (Fig. 4a; Supporting Information Table S4). Maxima of $V_{agg}$ at each level of turbulence also increased until turbulence reached the second highest level ($10^{-7} < \varepsilon$ $10^{-6}$ W kg$^{-1}$),
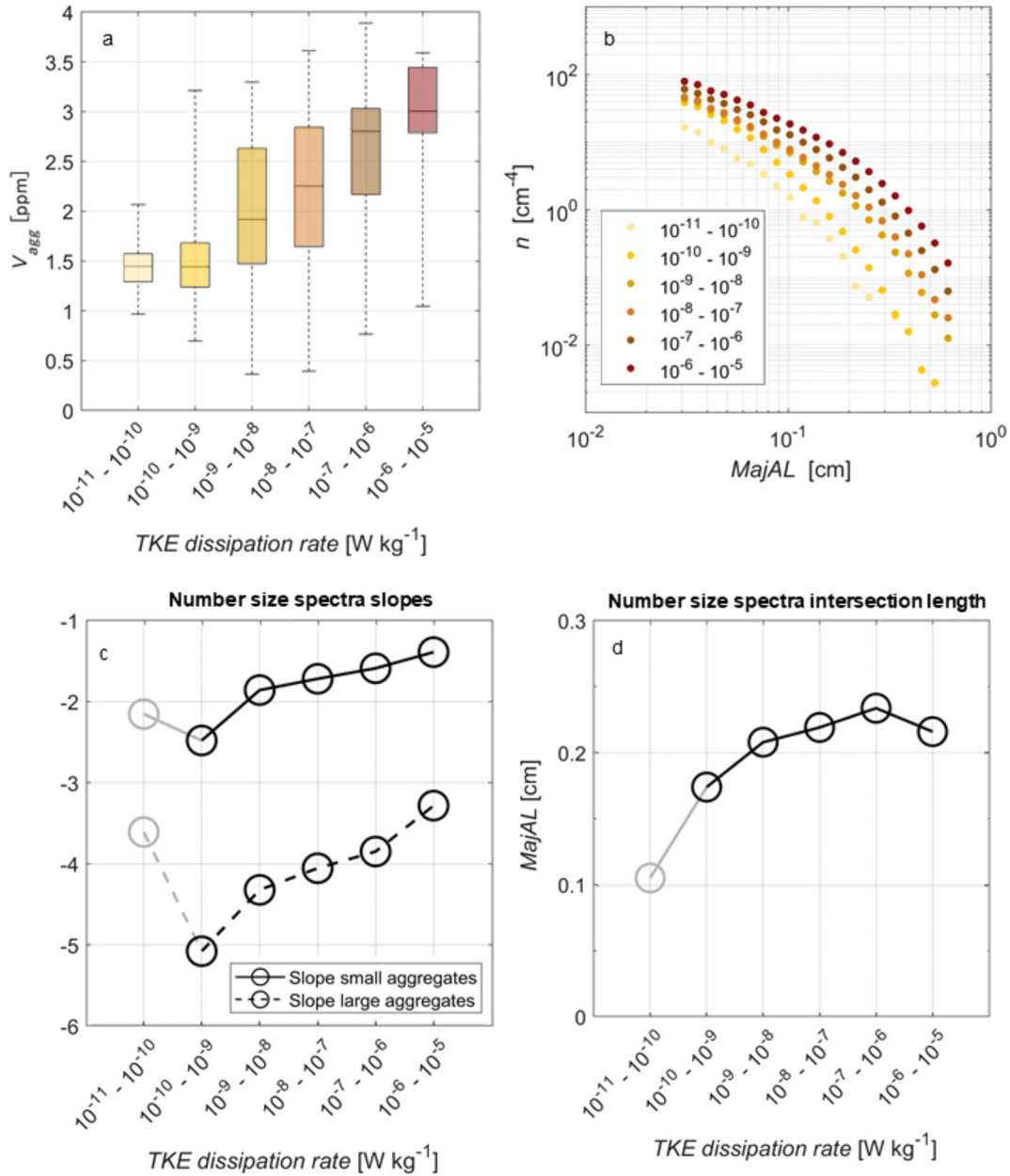


**Fig. 4.** Relationship between aggregate number size spectra in relation to different turbulence levels. (**a**) Total volume concentration of aggregates ($V_{agg}$, ppm) in log-10 scale across different levels of turbulence. The box color corresponds with the color indicated turbulence in Fig. 4b. (**b**) Number size spectra (*n*, cm$^{-4}$) for different turbulence levels ($\varepsilon$, *TKE dissipation rate* W kg$^{-1}$) as a function of size (*MajAL*, cm). Profiles from all sites were used to construct the spectra. Lighter colors indicate weaker turbulence and darker colors indicate stronger turbulence. (**c**) Relationship between turbulence and small and large aggregates slopes (solid and dashed lines, respectively). (**d**) Relationship between turbulence and the particle lengths where small and large aggregates slopes intersect. Gray points in panels c and d indicate points of lower confidence owing to incomplete particle size spectra. See Supporting Information Table S5 for details.

hereafter it decreased (Fig. 4a; Supporting Information Table S4).

Number size spectra slopes of both small and large aggregates became significantly flatter with increasing turbulence (small: $p = 0.02$, $R^2 = 0.88$, $n = 5$; large: $p < 0.01$, $R^2 = 0.95$, $n = 5$) (Fig. 4c; Supporting Information Table S5). Note that we excluded the weakest turbulence level ($10^{-11} < \varepsilon < 10^{-10}$ W kg$^{-1}$) from this correlation as we could not construct a complete number size spectrum for this range. We also observed the significant increase ($p = 0.04$, $R^2 = 0.80$, $n = 5$) in the intersection length of small and large aggregate slopes with increasing turbulence (from $MajAL = 0.11$–$0.23$ cm; Fig. 4d; Supporting Information Table S5). Site-specific number size spectra and average turbulence also showed the same trend: flatter slopes with increasing turbulence (small aggregates: $p = 0.03$, $R^2 = 0.68$, $n = 10$; large aggregates: $p = 0.11$, $R^2 = 0.54$, $n = 10$) and a shift in the intersection length toward larger sizes ($p < 0.01$, $R^2 = 0.61$, $n = 10$) (Supporting Information Fig. S5).

## Relationship between slopes and environmental parameters

Number size spectra slopes for both small and large aggregates correlated to varying degrees with the environmental factors. There was no significant correlation with either fluorescence, nonfluorescent turbidity (proxy for sediment load) or temperature for salinity, and there was no significant correlation when considering all sites. However, when excluding Lake Biwa (i.e., only marine sites), slopes for large aggregates were significantly steeper with increasing salinity ($p = 0.04$, $R^2 = 0.39$, $n = 9$; no significant correlation for small aggregates: $p = 0.09$, $R^2 = 0.27$, $n = 9$). Increasing turbidity resulted in significantly steeper slopes for both small aggregates ($p = 0.006$, $R^2 = 0.59$, $n = 10$) and large aggregates ($p = 0.03$, $R^2 = 0.37$, $n = 10$). Increases in both particle concentrations (for the size bin $MajAL = 1$ mm) and TKE dissipation rate were significantly associated with steeper slopes for small aggregates ($p = 0.03$, $R^2 = 0.41$, $n = 10$; $p = 0.003$, $R^2 = 0.64$, $n = 10$) but not for large aggregates ($p = 0.07$, $R^2 = 0.28$, $n = 10$; $p = 0.11$, $R^2 = 0.21$, $n = 10$).

Turbidity was significantly correlated with both TKE dissipation rate (positive correlation; $p = 0.03$, $R^2 = 0.41$, $n = 10$) and salinity when not considering Lake Biwa (negative correlation; $p < 0.05$, $R^2 = 0.37$, $n = 9$). Normalized aggregate abundance of number size spectra in the bins $MajAL = 0.3$ mm and $MajAL = 1$ mm was also significantly correlated with turbidity (respectively, $p < 0.001$, $R^2 = 0.79$, $n = 10$; $p < 0.001$, $R^2 = 0.82$, $n = 10$).

## Discussion

Comparison between our 10 contrasting locations suggested that aggregate dynamics showed consistent patterns in response to different levels of turbulence despite varying particle compositions and influence of the local ecosystems. The focus of our discussion is hence the effect of turbulence on aggregate sizes and strength, although we also explore potential confounding factors.

## Fundamental effects of turbulence on particle dynamics

Measured turbulence kinetic energy (TKE) dissipation rates ($10^{-11}$–$10^{-5}$ W kg$^{-1}$) span the typical range observed in most aquatic systems (excluding the surface and bottom boundary layers) (Bluteau et al. 2016; Smyth and Moum 2019). This agreement suggests our data likely represent the general characteristics of marine ecosystems. Consequently, we divided our dataset into levels of TKE dissipation rate, which we refer to as weak ($\sim 10^{-11}$ W kg$^{-1}$) to strong ($\sim 10^{-6}$ W kg$^{-1}$).

### *Interpreting changes to the size spectra slope under turbulence*

We observed flatter number size spectra slopes with increasing turbulence intensity, indicating relatively higher abundances of large aggregates compared to small ones, which can result from higher net aggregation rates. One explanation for this observation is the increased relative motion of particles, which directly increases aggregation rates (Jackson 1990). In addition, inertial particles tend to cluster in high strain regions (Squires and Eaton 1991; de Jong et al. 2010) which can increase aggregation rates by increasing particle concentration in the region.

Another potential explanation for our observations is the increase in aggregate strength in more turbulent environments, as shown by laboratory experiments and numerical models (Alldredge et al. 1990; Wang et al. 2011; Zahnow et al. 2011). In their numerical model, Zahnow et al. (2011) found that aggregate strength (determined as the force that bonds source particles together) increased with turbulence, leading to higher net aggregation rates. Similarly, Wang et al. (2011) observed in laboratory experiments that kaolinite clay formed smaller yet stronger aggregates (measured as the force that aggregate can withstand before disaggregation) under strong turbulence (shear 40–60 rpm). Although kaolinite clay may follow different aggregation processes than natural aggregates, other laboratory experiments using naturally collected aggregates also noted that strong aggregates can resist turbulence-driven disaggregation (Alldredge et al. 1990). This strength was attributed to their composition (high amounts of transparent exopolymer particles, TEP) and chemical changes associated with aging. While our study did not measure the chemical composition, the consistency between our results and these three studies supports the idea that aggregates in natural environments become stronger when turbulence increases.

Strongly bonded aggregates are likely more resistant to turbulence-driven disaggregation (Gmachowski 2002), leading to higher net aggregation and flatter slopes of the number size spectra. This mechanism may explain the flatter slopes as

turbulence levels increased (Fig. 4c; Supporting Information Fig. S5c). Flatter number size spectra, accompanied by an increase in aggregate strength (bonds of inner particles), were also observed in models (Zahnow et al. 2011).

Increasing turbulence has also been suggested to decrease the porosity of aggregates by filling spaces with small particles (Wang et al. 2011). Reduced porosity limits water flow through aggregates (Engel et al. 2009), possibly enhancing particle bonding (Jarvis et al. 2005) and hence leading to higher net aggregation (i.e., flatter slopes). Unfortunately, our image resolution is too low to explore any changes in porosity.

Finally, the dominant disaggregation mechanism likely changes as turbulence increases, from "surface erosion" to "splitting," which both produce different sizes of aggregates. Typically, surface erosion occurs at weaker shear force (turbulence) and produces a large number of small aggregates, while "splitting" occurs at stronger shear force and produces relatively large aggregates (Spicer and Pratsinis 1996; Zahnow et al. 2011). Hence, as turbulence levels increase and splitting becomes the predominant disaggregation mechanism, the resulting production of relatively large aggregates would lead to flatter number size spectra slopes.

### Size spectra intersection length indicates resistance to turbulence-driven disaggregation

Another feature of our number size spectra was the shift in the aggregate length where small and large aggregate slopes intersect (Fig. 4d). We carried out a literature review and found that several studies indicate a change in slope, though the authors did not fit it (Iversen et al. 2010; Forest et al. 2012; Roullier et al. 2014). We found only one study where the authors fit a split slope to particles imaged in the deep ocean (> 2000 m depth) across the Atlantic and Arctic (Bochdansky et al. 2016). Intriguingly, the slopes showed the opposite to our observations (i.e., large-aggregate slope is flatter), which was explained by a disproportionate abundance of larger (> 379 $\mu$m) aggregates that were amorphous, porous, and contained large amounts of TEP (Bochdansky et al. 2016). We speculate that the difference between their observations and ours may be because we investigated shallow profiles that include the euphotic zone, where most of the particle production occurs. Our profiles hence are more likely to capture source particles and particle populations that formed via aggregation (in the sense explained in our introduction), while the particles in deep profiles may undergo different dynamics, such as a prevalence in collision-based aggregation. Deep-ocean size spectra are also likely heavily influenced by the influx and outflux of sinking particles ("marine snow"), microbial activity and self-assembly of gels (Verdugo et al. 2008; Bochdansky et al. 2016), a reduced level of fragmentation by zooplankton and fish (e.g., Vinogradov and Tseitlin 1983), and reduced exposure to disaggregation-causing turbulence levels (Thorpe 2005).

We observed the split slopes at all turbulence levels, indicating that they are a universal feature of our number size spectra. The immediate question that arises is: why is there a change in net aggregation at a certain aggregate size (independent of the turbulence level)?

The number size spectra intersection length indicates an aggregate size at which the balance between aggregation and disaggregation changes (i.e., disaggregation becomes more critical), resulting in a notable decrease in large-aggregate abundance. A possible explanation is that large aggregates tend to be more porous (Logan and Hunt 1987; Logan and Wilkinson 1990) and have a higher fractal dimension (Burd and Jackson 2009; Zahnow et al. 2011). For aggregates formed in natural environments, their source particles are typically diverse with different shapes and sizes. As aggregates "grow," they are hence likely to combine a multitude of different source particle types, which - compared to, for example, relatively uniform clay particles - do not pack neatly, leaving more space and ultimately leading to higher porosity. In addition, the disordered arrangement of source particles likely results in weaker bonding as many of the bonding forces (van der Waals forces, Lewis acid–base forces, electrostatic repulsions) are both size and distance dependent (Song et al. 2023). Indeed, larger aggregates have been shown to be generally weaker (albeit based on mineral aggregates) (Hamm 2002; Maggi and Tang 2015). This increased weakness of large aggregates could shift the balance between aggregation and disaggregation toward disaggregation.

Another explanation for the different net aggregation behaviors of "large" vs. "small" particles could be the fluid dynamics. The smallest size of eddies that exist in a turbulent flow (expressed as Kolmogorov length scale) is dependent on the turbulence level. Observations of sediment flocs showed that flocs larger than the Kolmogorov length scale are more likely to disaggregate in response to turbulence (Braithwaite et al. 2012). Natural aggregates like those in our study likely follow the same behavior, with aggregates larger than the Kolmogorov length scale experiencing higher rates of disaggregation. The consequence would be a change in the slope of the number size spectra at the particle size corresponding to the Kolmogorov length scale. For our turbulence range, the Kolmogorov length scale ranged from 0.06 to 1.8 cm (at TKE dissipation rate = $10^{-5}$ and $10^{-11}$ W kg$^{-1}$, respectively). Though the particle length where small and large particle slopes intersect (0.11–0.23 cm) falls within this Kolmogorov length scale range, the latter is much broader. Moreover, our size spectra intersection lengths shifted toward larger aggregates with increasing turbulence levels (Fig. 5d), which is the opposite trend expected if the change in aggregate dynamics was purely driven by the Kolmogorov length scale (Braithwaite et al. 2012).

We suggest that the number size spectra intersection length increases under stronger turbulence as a consequence of the
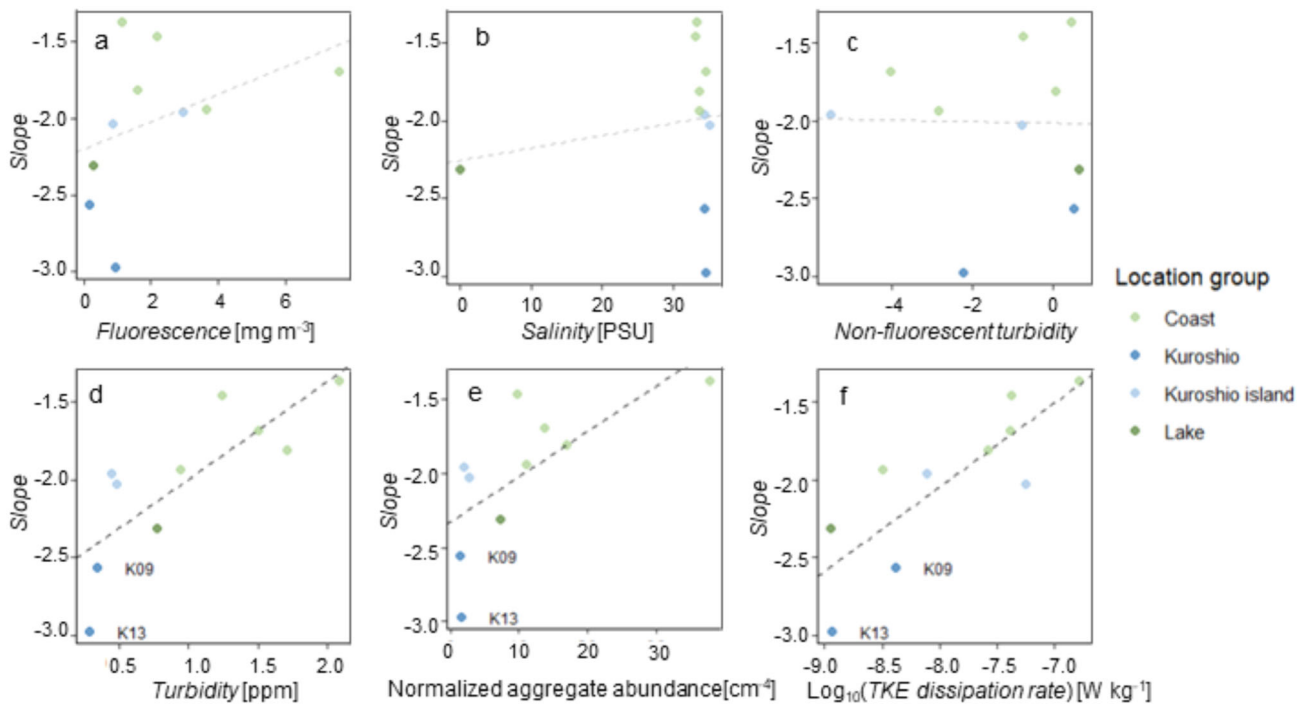
**Fig. 5.** Relationship between the slope of the number size spectra ("small aggregates") and (**a**) total fluorescence, (**b**) salinity, (**c**) nonfluorescent turbidity, (**d**) turbidity, (**e**) normalized aggregate abundance with a *MajAL* of 1 mm, and (**f**) turbulence. Dashed lines show regression line, where gray lines are not significant (**a**–**c**), and black lines are significant (**d**–**f**). Regression statistics are listed in the "Results" section. Colors indicate location–group as in Fig. 1. The two offshore Kuroshio sites are highlighted with labels "K09" and "K13."

more strongly bonded aggregates (*see* previous section). If this strength perpetuates through the number size spectra, the resulting aggregate population is relatively more resistant to turbulence-driven disaggregation than those formed under weaker turbulence. Subsequently, the aggregate size at which net aggregation changes would shift toward larger aggregates. Note that this conclusion is based on number size spectra compiled across different sites, and does not follow a specific "cohort" of particles like single-site profiles or laboratory-based aggregation experiments. Our results hence point to general characteristics of natural aggregates.

**Confounding environmental factors affecting size spectra**

Our data were collected over a wide range of environments. We hence expect many factors other than turbulence to influence the number size spectra, including those we did not measure in our study, and three that we did measure and explore in more detail: chlorophyll *a* (Chl *a*) concentration, sediment load, and salinity.

Chlorophyll *a* concentrations (a proxy for phytoplankton abundance) were previously observed to lead to flatter number size spectra, suggesting that relatively higher net aggregation occurs when phytoplankton abundance is high (Buonassissi and Dierssen 2010). This trend may be due to higher Chl *a* concentrations indicating larger phytoplankton sizes (references in Buonassissi and Dierssen 2010). We also observed generally flatter slopes at the coastal sites,

where Chl *a* fluorescence concentrations were relatively high and likely dominated by larger phytoplankton (Han and Furuya 2000; Ramaiah and Furuya 2002; Tachibana et al. 2016), compared to the offshore Kuroshio sites, where Chl *a* fluorescence concentrations were lower and phytoplankton is typically dominated by nanoplankton and picoplankton (Clayton et al. 2014). However, there was no significant correlation between average total fluorescence and the number size spectra slopes for either small or large aggregates. A similar lack of correlation in a coastal study, conducted approximately 10 km offshore of California in water-column depths between 250 and 450 m (Franks and Jaffe 2008), was partly attributed to too few particles to construct full number size spectra. In contrast, we observed sufficient particle numbers across all sites, strengthening our conclusion that net aggregation across our sampling region was determined by factors other than Chl *a* fluorescence alone.

Working in the opposite direction to phytoplankton abundance, high concentrations of sediments have been shown to facilitate disaggregation (i.e., steeper number size spectra) (Passow and De La Rocha 2006). Our proxy for sediment load ("nonfluorescent turbidity") did not correlate with number size spectra slopes, indicating a minor role of nonfluorescent turbidity on disaggregation.

Salinity has been directly linked to net aggregation, with increasing net aggregation (i.e., flatter slopes) along a salinity

gradient from an estuary toward the open ocean (Mari et al. 2012). This change in aggregation dynamics was attributed to a change in the sticking properties of TEP (Mari et al. 2012), which appeared to be influenced directly by salinity through changes in the molecular bonding of TEP (Passow 2002; Wetz et al. 2009; but *see* also Meng and Liu 2016). However, our data did not indicate a convincing trend: the number size spectra slopes in the freshwater lake were similar to marine sites, and higher net aggregation (albeit not significantly different) was observed at the fresher sites, contrary to expectations. One explanation is that the relatively narrow salinity range at our marine sites (33–35 PSU) may be insufficient to show salinity effects. Alternatively, the fresher sites had stronger turbulence, which can increase TEP production (Burns et al. 2019). Thus, the impact of salinity on aggregate dynamics may be masked by stronger turbulence at our coastal sites.2009

Finally, there are other, particularly biological and physical, factors that may play a role, such as species composition (Simon et al. 2002; Grossart et al. 2006), phytoplankton growth phase (Alldredge and Gotschalk 1989; Kiørboe et al. 1994), TEP production (Burns et al. 2019), density gradients (Prairie et al. 2019), and biologically mediated fragmentation of aggregates (Dilling and Alldredge 2000; Dilling and Brzensinski 2004; Kimura et al. 2024). In the Kuroshio, the number size spectra slopes were steeper than expected based on the linear regressions between slope and turbidity, particle concentration and TKE dissipation rate (Fig. 5d–f). We propose that intermittent turbulence in the Kuroshio (Nagai et al. 2019) supports a responsive ecosystem characterized by rapidly growing large phytoplankton (e.g., diatom) and a predominantly herbivorous zooplankton community (Nakata and Hidaka 2003). The resulting spectrum would be steep, indicative of high net disaggregation or a short food web structure (Platt and Denman 1977; Silvert and Platt 1978). Sporadic growth of large phytoplankton is supported by our observations of frequent fluorescent spikes (Fig. 3), which contrasts the prevailing view of nanoplankton and picoplankton dominating these waters (Clayton et al. 2014). The rapid loss of aggregates (i.e., steep slopes) then points toward biologically mediated fragmentation by herbivorous zooplankton and fish (Dilling and Alldredge 2000; Dilling and Brzensinski 2004). Our data hence help to explain the "Kuroshio paradox" (Sogawa et al. 2019) and why this region is a key spawning ground for many fish species despite its oligotrophic nutrient conditions and relatively little food (Saito 2019).

## Data availability statement

All data used in this study are available from the corresponding author (MT) upon request to marika.takeuchi@noc.ac.uk.

## References

Alldredge, A. 1998. The carbon, nitrogen and mass content of marine snow as a function of aggregate size. Deep-Sea Res. I Oceanogr. Res. Pap. **45**: 529–541.

Alldredge, A. L., and M. W. Silver. 1988. Characteristics, dynamics and significance of marine snow. Prog. Oceanogr. **20**: 41–82.

Alldredge, A. L., and C. Gotschalk. 1989. Direct observations of the mass flocculation of diatom blooms: Characteristics, settling velocities and formation of diatom aggregates. Deep-Sea Res. A Oceanogr. Res. Pap. **36**: 159–171.

Alldredge, A. L., T. C. Granata, C. C. Gotschalk, and T. D. Dickey. 1990. The physical strength of marine snow and its implications for particle disaggregation in the ocean. Limnol. Oceanogr. **35**: 1415–1428.

Alldredge, A. L., U. Passow, and H. D. Haddock. 1998. The characteristics and transparent exopolymer particle (TEP) content of marine snow formed from thecate dinoflagellates. J. Plankton Res. **20**: 393–406.

Arakawa, H., T. Shimoda, and T. Morinaga. 2003. Outflow and inflow of suspended particles at the mouth of Tokyo Bay. J. Tokyo Univ. Fish. **89**: 23–35.

Blanchard, J. L., R. F. Heneghan, J. D. Everett, R. Trebilco, and A. J. Richardson. 2017. From bacteria to whales: Using functional size spectra to model marine ecosystems. Trends Ecol. Evol. **32**: 174–186.

Bluteau, C. E., N. L. Jones, and G. N. Ivey. 2016. Acquiring long-term turbulence measurements from moored platforms impacted by motion. J. Atmos. Oceanic Tech. **33**: 2535–2551.

Bochdansky, A. B., M. A. Clouse, and G. J. Herndl. 2016. Dragon kings of the deep sea: Marine particles deviate markedly from the common number-size spectrum. Sci. Rep. **6**: 22633.

Braithwaite, K. M., D. G. Bowers, W. A. M. Nimmo Smith, and G. W. Graham. 2012. Controls on floc growth in an energetic tidal channel. J. Geophys. Res. Oceans **117**: 1–12.

Briggs, N., G. Dall'Olmo, and H. Claustre. 2020. Major role of particle fragmentation in regulating biological sequestration of $CO_2$ by the oceans. Science **367**: 791–793.

Briggs, N., and others. 2011. High-resolution observations of aggregate flux during a sub-polar North Atlantic spring bloom. Deep-Sea Res. I Oceanogr. Res. Pap. **58**: 1031–1039.

Buesseler, K. O., and P. W. Boyd. 2009. Shedding light on processes that control particle export and flux attenuation in the twilight zone of the open ocean. Limnol. Oceanogr. **54**: 1210–1232.

Buonassissi, C. J., and H. M. Dierssen. 2010. A regional comparison of particle size distributions and the power law approximation in oceanic and estuarine surface waters. Journal of Geophysical Research: Oceans **115**. doi:10.1029/2010jc006256

Burd, A. B., and G. A. Jackson. 2009. Particle aggregation. Ann. Rev. Mar. Sci. **1**: 65–90.

Burns, W. G., A. Marchetti, and K. Ziervogel. 2019. Enhanced formation of transparent exopolymer particles (TEP) under turbulence during phytoplankton growth. J. Plankton Res. **41**: 349–361. doi:10.1093/plankt/fbz018

Chow, S., and others. 2019. Molecular diet analysis of *Anguilliformes leptocephalus* larvae collected in the western North Pacific. PLoS One **14**: e0225610.

Clayton, S., T. Nagai, and M. J. Follows. 2014. Fine scale phytoplankton community structure across the Kuroshio Front. J. Plankton Res. **36**: 1017–1030.

de Jong, J., J. P. L. C. Salazar, S. H. Woodward, L. R. Collins, and H. Meng. 2010. Measurement of inertial particle clustering and relative velocity statistics in isotropic turbulence using holographic imaging. Int. J. Multiphase Flow **36**: 324–332. doi:10.1016/j.ijmultiphaseflow.2009.11.008

Dilling, L. and M. A. Brzenzinski. 2004. Quantifying marine snow as a food choice for zooplankton using stable silicon isotope tracers. J. Plankton Res. **26**: 1105–1114.

Dilling, L., and A. L. Alldredge. 2000. Fragmentation of marine snow by swimming macrozooplankton: A new process impacting carbon cycling in the sea. Deep-Sea Res. I Oceanogr. Res. Pap. **47**: 1227–1245.

Dissanayake, A. L., A. B. Burd, K. L. Daly, S. Francis, and U. Passow. 2018. Numerical modeling of the interactions of oil, marine snow, and riverine sediments in the ocean. J. Geophys. Res. Oceans **123**: 5388–5405.

Doubell, M. J., H. Yamazaki, H. Li, and Y. Kokubu. 2009. An advanced laser-based fluorescence microstructure profiler (TurboMAP-L) for measuring bio-physical coupling in aquatic systems. J. Plankton Res. **31**: 1441–1452.

Ducklow, H. W. 2001. Upper Ocean carbon export and the biological pump. Oceanography **14**: 50–54.

Engel, A., J. Szlosek, L. Abramson, Z. Liu, and C. Lee. 2009. Investigating the effect of ballasting by CaCO3 in Emiliania huxleyi: I. Formation, settling velocities and physical properties of aggregates. Deep Sea Research Part II: Topical Studies in Oceanography **56**: 1396–1407. doi:10.1016/j.dsr2.2008.11.027

Falkowski, P. G., R. R. Barber, and V. Smetacek. 1998. Biogeochemical controls and feedbacks on ocean primary production. Science **281**: 200–206.

Foloni-Neto, H., R. Lueck, Y. Mabuchi, H. Nakamura, M. Arima, and H. Yamazaki. 2014. A new quasi-horizontal glider to measure biophysical microstructure. J. Atmos. Ocean. Tech. **31**: 2278–2293.

Foloni-Neto, H., M. Tanaka, H. Joshima, and H. Yamazaki. 2016. A comparison between quasi-horizontal and vertical observations of phytoplankton microstructure. J. Plankton Res. **38**: 993–1005.

Forest, A., and others. 2012. Size distribution of particles and zooplankton across the shelf-basin system in southeast Beaufort Sea: Combined results from an underwater vision profiler and vertical net tows. Biogeosciences **9**: 1301–1320.

Franks, P. J. S., and J. S. Jaffe. 2001. Microscale distributions of phytoplankton: Initial results from a two-dimensional imaging fluorometer, OSST. Mar. Ecol. Prog. Ser. **220**: 59–72.

Franks, P. J. S., and J. S. Jaffe. 2008. Microscale variability in the distributions of large fluorescent particles observed in situ with a planar laser imaging fluorometer. J. Mar. Syst. **69**: 254–270.

Geyer, W. R., M. E. Scully, and D. K. Ralston. 2008. Quantifying vertical mixing in estuaries. Environ. Fluid Mech. **8**: 495–509.

Giering, S. L. C., and others. 2014. Reconciliation of the carbon budget in the ocean's twilight zone. Nature **507**: 480–483. doi:10.1038/nature13123

Gmachowski, L. 2002. Aggregate structure and size distribution at steady state shear aggregation. Colloids Surf. A Physicochem. Eng. Asp. **201**: 41–46.

Grossart, H.-P., G. Czub, and M. Simon. 2006. Algae–bacteria interactions and their effects on aggregation and organic matter flux in the sea. Environ. Microbiol. **8**: 1074–1084. doi:10.1111/j.1462-2920.2006.00999.x

Hasegawa, T., I. Koike, and H. Mukai. 2001. Fate of food nitrogen in marine copepods. Marine Ecology Progress Series **210**: 167–174. doi:10.3354/meps210167

Hamm, C. E. 2002. Interactive aggregation and sedimentation of diatoms and clay-sized lithogenic material. Limnol. Oceanogr. **47**: 1790–1795.

Han, M.-S., and K. Furuya. 2000. Size and species-specific primary productivity and community structure of phytoplankton in Tokyo Bay. J. Plankton Res. **22**: 1221–1235.

Iversen, M. H., N. Nowald, H. Ploug, G. A. Jackson, and G. Fischer. 2010. High resolution profiles of vertical particulate organic matter export off Cape Blanc, Mauritania: Degradation processes and ballasting effects. Deep-Sea Res. I Oceanogr. Res. Pap. **57**: 771–784.

Jackson, G. A. 1990. A model of the formation of marine algal flocs by physical coagulation processes. Deep-Sea Res. A Oceanogr. Res. Pap. **37**: 1197–1211.

Jarvis, P., B. Jefferson, J. Gregory, and S. A. Parsons. 2005. A review of floc strength and breakage. Water Res. **39**: 3121–3137.

Khelifa, A., and P. S. Hill. 2017. Models for effective density and settling velocity of flocs models for effective density and settling velocity of flocs models pour la densité effective et la vitesse de sédimentation de flocs. J. Hydraul. Res. **44**: 309–401.

Kimura, S., and others. 2024. Distribution and stable isotope ratio characteristics of Japanese eel leptocephali in relation to hydrographic structure of their Pacific Ocean spawning area. Fisheries Oceanography. Fish. Oceanogr. **33**: e12671.

Kiørboe, T., C. Lundsgaard, M. Olesen, and J. L. S. Hansen. 1994. Aggregation and sedimentation processes during a

spring phytoplankton bloom: A field experiment to test coagulation theory. J. Mar. Res. **52**: 297–323.

Kokubu, Y., H. Yamazaki, T. Nagai, and E. S. Gross. 2013. Mixing observations at a constricted channel of a semi-closed estuary: Tokyo Bay. Cont. Shelf Res. **69**: 1–16.

Kwong, L. E., and E. A. Pakhomov. 2021. Zooplankton size spectra and production assessed by two different nets in the subarctic Northeast Pacific. J. Plankton Res. **43**: 527–545.

Larson, E., and A. L. Shanks. 1996. Consumption of marine snow by two species of juvenile mullet and its contribution to their growth. Mar. Ecol. Prog. Ser. **130**: 19–28.

Li, X. Y., J. J. Zhang, and J. H. Lee. 2004. Modelling particle size distribution dynamics in marine waters. Water Res. **38**: 1305–1317.

Logan, B. E., and J. R. Hunt. 1987. Advantages to microbes of growth in permeable aggregates in marine systems. Limnol. Oceanogr. **32**: 1034–1048.

Logan, B. E., and D. B. Wilkinson. 1990. Fractal geometry of marine snow and other biological aggregates. Limnol. Oceanogr. **35**: 130–136.

Logan, B. E., and J. R. Kilps. 1995. Fractal dimensions of aggregates formed in different fluid mechanical environments. Water Res. **29**: 443–453.

Lampitt, R. S., T. Noji, and B. von Bodungen. 1990. What happens to zooplankton faecal pellets? Implications for material flux. Marine Biology **104**: 15–23. doi:10.1007/bf01313152

Lombard, F., and others. 2019. Globally consistent quantitative observations of planktonic ecosystems. Front. Mar. Sci. **6**: 196.

Maggi, F., and F. H. M. Tang. 2015. Analysis of the effect of organic matter content on the architecture and sinking of sediment aggregates. Mar. Geol. **363**: 102–111.

Mari, X., and others. 2012. Aggregation dynamics along a salinity gradient in the Bach Dang estuary, North Vietnam. Estuar. Coast. Shelf Sci. **96**: 151–158.

Masunaga, E., R. S. Arthur, O. B. Fringer, and H. Yamazaki. 2017. Sediment resuspension and the generation of intermediate nepheloid layers by shoaling internal bores. J. Mar. Syst. **170**: 31–41.

McCave, I. N. 1984. Size spectra and aggregation of suspended particles in the deep ocean. Deep-Sea Res. A Oceanogr. Res. Pap. **31**: 329–352.

Meng, S., and Y. Liu. 2016. New insights into transparent exopolymer particles (TEP) formation from precursor materials at various $Na^+/Ca^{2+}$ ratios. Sci. Rep. **6**: 19747. doi:10.1038/srep19747

Møller, E., P. Thor, and T. Nielsen. 2003. Production of DOC by Calanus finmarchicus, *C. glacialis* and *C. hyperboreus* through sloppy feeding and leakage from fecal pellets. Marine Ecology Progress Series **262**: 185–191. doi:10.3354/meps262185

Möller, K. O., and others. 2012. Marine snow, zooplankton and thin layers: Indications of a trophic link from small-scale sampling with the Video Plankton Recorder. Mar. Ecol. Prog. Ser. **468**: 57–69.

Nagai, T., H. Saito, K. Suzuki, and M. Takahashi. 2019. Kuroshio current physical, biologeochemical, and ecosystem dynamics. AGU-Wiley.

Nakata, K., and K. Hidaka. 2003. Decadal-scale variability in the Kuroshio marine ecosystem in winter. Fish. Oceanogr. **12**: 234–244.

Nasmyth, P. 1970. Oceanic Turbulence. p. 69. Ph.D. thesis, Univ. of British Columbia.

Omand, M. M., R. Govindarajan, J. He, and A. Mahadevan. 2020. Sinking flux of particulate organic matter in the oceans: Sensitivity to particle characteristics. Scientific Reports **10**. doi:10.1038/s41598-020-60424-5

Passow, U. 2002. Production of transparent exopolymer particles (TEP) by phyto- and bacterioplankton. Mar. Ecol. Prog. Ser. **236**: 1–12.

Passow, U., and C. L. De La Rocha. 2006. Accumulation of mineral ballast on organic aggregates. Global Biogeochem. Cycles **20**: GB1013.

Petrik, C. M., G. A. Jackson, and D. M. Checkley. 2013. Aggregates and their distributions determined from LOPC observations made using an autonomous profiling float. Deep-Sea Res. I Oceanogr. Res. Pap. **74**: 64–81.

Platt, T., and K. Denman. 1977. Organisation in the pelagic ecosystem. Helgoländ. Wiss. Meer. **30**: 575–581.

Prairie, J. C., Q. W. Montgomery, K. W. Proctor, and K. S. Ghiorso. 2019. Effects of phytoplankton growth phase on settling properties of marine aggregates. J. Mar. Sci. Eng. **7**: 265. doi:10.3390/jmse7080265

Ramaiah, N., and K. Furuya. 2002. Seasonal variations in phytoplankton composition and transparent exopolymer particles in a eutrophicated coastal environment. Aquat. Microb. Ecol. **30**: 69–82.

Roullier, F., and others. 2014. Particle size distribution and estimated carbon flux across the Arabian Sea oxygen minimum zone. Biogeosciences **11**: 4541–4557.

Saito, H. 2019. The Kuroshio. The Kuroshio its region, scientific acticities and emerging issues. 1–11. AGU-Wiley

Sogawa, S., K. Hidaka, Y. Kamimura, M. Takahashi, H. Saito, Y. Okazaki, Y. Shimizu, and T. Setou. 2019. Environmental characteristics of spawning and nursery grounds of Japanese sardine and mackerels in the Kuroshio and Kuroshio Extension area. Fisheries Oceanography **28**: 454–467. doi:10.1111/fog.12423

Silvert, W., and T. Platt. 1978. Energy flux in the pelagic ecosystem: A time-dependent equation. Limnol. Oceanogr. **23**: 813–816.

Simon, M., H. P. Grossart, B. Schweitzer, and H. Ploug. 2002. Microbial ecology of organic aggregates in aquatic ecosystems. Aquat. Microb. Ecol. **28**: 175–211.

Smyth, W. D., and J. N. Moum. 2019. 3D turbulence, p. 486–496. *In* H. Bokuniewicz, P. Yger, and J. Kirk Cochran [eds.], Encyclopedia of ocean sciences. Academic Press.

Song, Y., A. B. Burd, and M. J. Rau. 2023. The deformation of marine snow enables its disaggregation in simulated oceanic shear. Front. Mar. Sci. **10**: 1224518.

Spicer, P. T., and S. E. Pratsinis. 1996. Coagulation and fragmentation: Universal steady-state particle-size distribution. AIChE J. **42**: 1612–1620.

Squires, K. D., and J. K. Eaton. 1991. Preferential concentration of particles by turbulence. Phys. Fluids **3**: 1169–1178. doi:10.1063/1.858045

Steinberg, D., N. Nelson, C. Carlson, and A. Prusak. 2004. Production of chromophoric dissolved organic matter (CDOM) in the open ocean by zooplankton and the colonial cyanobacterium *Trichodesmium spp*. Marine Ecology Progress Series **267**: 45–56. doi:10.3354/meps267045

Tachibana, A., Y. Nishibe, H. Fukuda, K. Kawanobe, and A. Tsuda. 2016. Phytoplankton community structure in Otsuchi Bay, northeastern Japan, after the 2011 off the Pacific coast of Tohoku Earthquake and tsunami. J. Oceanogr. **73**: 55–65.

Takeuchi, M., M. J. Doubell, G. A. Jackson, M. Yukawa, Y. Sagara, and H. Yamazaki. 2019. Turbulence mediates marine aggregate formation and destruction in the upper ocean. Sci. Rep. **9**: 16280.

Thorpe, S. A. 2005. The turbulent ocean. Cambridge Univ. Press.

Tsugeki, N. K., J. Urabe, Y. Hayami, M. Kuwae, and M. Nakanishi. 2009. Phytoplankton dynamics in Lake Biwa during the 20th century: Complex responses to climate variation and changes in nutrient status. J. Paleolimnol. **44**: 69–83.

Tsukamoto, K., and M. J. Miller. 2020. The mysterious feeding ecology of leptocephali: A unique strategy of consuming marine snow materials. Fish. Sci. **87**: 11–29.

Turner, J. T. 2015. Zooplankton fecal pellets, marine snow, phytodetritus and the ocean's biological pump. Prog. Oceanogr. **130**: 205–248.

Verdugo, P., and others. 2008. Marine biopolymer self-assembly: Implications for carbon cycling in the ocean. Faraday Discuss. **139**: 393–398.

Vinogradov, M. E., and V. B. Tseitlin. 1983. Deep-sea pelagic domain, p. 123–165. *In* G. C. Rowe [ed.], Deep-sea biology. Ch. 4, v. **8**. Wiley.

Wang, D., R. Wu, Y. Jiang, and C. W. K. Chow. 2011. Characterization of floc structure and strength: Role of changing shear rates under various coagulation mechanisms. Colloids Surf. A Physicochem. Eng. Asp. **379**: 36–42.

Wetz, M. S., M. C. Robbins, and H. W. Paerl. 2009. Transparent exopolymer particles (TEP) in a river-dominated estuary: Spatial–temporal distributions and an assessment of controls upon TEP formation. Estuar. Coasts **32**: 447–455.

Winterwerp, J. C. 2002. On the flocculation and settling velocity of estuarine mud. Cont. Shelf Res. **22**: 1339–1360.

Wolk, F., L. Seuront, and H. Yamazaki. 2001. Spatial resolution of a new micro-optical probe for chlorophyll and turbidity. J. Tokyo Univ. Fish. **87**: 13–21.

Wolk, F., H. Yamazaki, L. Seuront, and R. G. Lueck. 2002. A new free-fall profiler for measuring biophysical microstructure. J. Atmos. Oceanic Tech. **19**: 780–793.

Wolk, F., H. Yamazaki, H. Li, and R. G. Lueck. 2006. Calibrating the spatial response of bio-optical sensors. J. Atmos. Oceanic Tech. **23**: 511–516.

Zahnow, J. C., J. Maerz, and U. Feudel. 2011. Particle-based modeling of aggregation and fragmentation processes: Fractal-like aggregates. Phys. D Nonlinear Phenomena **240**: 882–893.

## Acknowledgments

## Conflict of Interest

The authors declare no conflicts of interest.